AIAA JOURNAL
Vol. 47, No. 1, January 2009

Procedure to Validate Direct Numerical Simulations of Wall-Bounded Turbulence Including Finite-Rate Reactions

Lian Duan* and M. Pino Martín†
Princeton University, Princeton, New Jersey 08544

DOI: 10.2514/1.38318

This paper first discusses the constitutive relations and surface catalytic model for direct numerical simulation of wall-bounded turbulence including finite-rate chemistry and gas–surface interaction and then provides a systematic procedure to test the validity of the simulations by dividing the whole problem into different components and testing each component separately. Namely, comparisons against similarity solutions and other established hypersonic boundary-layer solutions are used to test the validity of laminar mean flow with and without gas-phase chemical reactions; comparisons against the analytic solution for the one-dimensional diffusion equation are used to test the validity of the surface catalysis boundary condition; and comparisons against empirical predictions, detailed experimental data and linear stability theory are used to test the validity of turbulent boundary-layer solutions.

c_p = specific heat at constant pressure, $J/(kg \cdot K)$
c_v = specific heat at constant volume, $J/(kg \cdot K)$
E = total energy, J/m^3
E_v = vibrational energy, J/m^3
h = specific enthalpy, J/kg
h° = heat of formation, J/kg
K_{eq} = Equilibrium constant
k_B = Boltzmann's constant, 1.381×10^{-23} J/K
k_b = backward reaction coefficient
k_f = forward reaction coefficient
M = molecular weight, kg/mole
N_A = Avogadro's number, 6.022×10^{23} $mole^{-1}$
p = pressure $[\Sigma_s \rho_s (\hat{R}/M_s)T]$, Pa
q = heat flux $[-\kappa(\partial T/\partial x_j)]$, $J/(m^2 \cdot s)$
S_{ij} = Strain rate tensor $[\frac{1}{2}(\partial u_i/\partial x_j + \partial u_j/\partial x_i)]$, s^{-1}
T = translational temperature, K
u = velocity, m/s
v = diffusion velocity, m/s
$\bar{v}$ = average thermal velocity, m/s
w = production rate, $kg/(m^3 \cdot s)$
x = spatial coordinate along streamwise direction, m
y = spatial coordinate along wall-normal direction for two-dimensional flows, m
z = spatial coordinate along wall-normal direction for three-dimensional turbulent flows, m
γ = heat capacity ratio or catalytic recombination coefficient
$\hat{R}$ = universal gas constant, $8.314 J/(mole \cdot K)$
θ_v = vibrational temperature, K
κ = mixture thermal conductivity, $J/(K \cdot m \cdot s)$
μ = mixture viscosity, $kg/(m \cdot s)$
ρ = density, kg/m^3
σ_{ij} = shear stress tensor $(2\mu S_{ij} - \frac{2}{3}\mu\delta_{ij}S_{kk})$, Pa

Subscripts

i, j = Cartesian coordinate directions or species
s = species variable
w = wall quantity

Received 29 April 2008; revision received 15 August 2008; accepted for publication 28 August 2008.

*Ph.D. Student, Department of Mechanical and Aerospace Engineering. Student Member AIAA.
†Assistant Professor, Department of Mechanical and Aerospace Engineering. Senior Member AIAA.

I. Introduction

THE boundary layers that are formed on hypersonic vehicles are hot, chemically reacting, and turbulent. Currently, the boundary layer on realistic hypersonic vehicles is simulated either assuming that the boundary layer is laminar or using simple models that have not been calibrated for hypersonic applications. Generally, the calibration of turbulent models has been done using direct numerical simulation (DNS) databases of incompressible flows or using perfect-gas wind-tunnel data. As a result, the chemical composition of gas, the skin friction, and the heat transfer are not predicted accurately. If we were able to perform accurate simulations of hypersonic flows, we might find a different chemical composition of the gas and different heating rates than those that are currently predicted.

Direct numerical simulations including high-temperature physics can be used to study the interaction of finite-rate reactions, heat transfer, and surface catalysis and to develop and assess turbulence models. However, detailed experimental data of high-temperature supersonic or hypersonic turbulent boundary layers to validate DNS data do not currently exist, and exact solutions for the problem are not possible. For this reason, testing the validity of such simulations requires separately testing different components of the whole problem.

This paper first describes the constitutive relations and numerical methods for direct numerical simulation (DNS) of wall-bounded turbulence, including real-gas effects and wall catalysis, and then provides a systematic procedure for validating codes of this category. The validation includes mean flowfield, surface catalytic boundary condition, and turbulence. The mean flowfield is validated against a similarity solution and solutions are provided by data-parallel line relaxation (DPLR) [1], which is a parallel multiblock finite volume code that solves the Navier–Stokes equations, including finite-rate chemistry and the effects of thermal nonequilibrium. The wall catalysis boundary condition is tested using the analytic solution to the one-dimensional diffusion equation. The turbulence field is validated against theoretical results and experimental data. When describing the validation procedure, the validation of our DNS code is used as an example to show the effectiveness of the procedure.

II. Governing Equations and Constitutive Relations

The equations describing the unsteady motion of a reacting fluid are given by the species mass, mass-averaged momentum, and total-energy-conservation equations, which, neglecting thermal non-equilibrium, are

$$\frac{\partial \rho_s}{\partial t} + \frac{\partial}{\partial x_j}(\rho_s u_j + \rho_s v_{sj}) = w_s$$
$$\frac{\partial \rho u_i}{\partial t} + \frac{\partial}{\partial x_j}(\rho u_i u_j + p\delta_{ij} - \sigma_{ij}) = 0 \quad (1)$$
$$\frac{\partial E}{\partial t} + \frac{\partial}{\partial x_j}\left((E+p)u_j - u_i\sigma_{ij} + q_j + \sum_s \rho_s v_{sj} h_s\right) = 0$$

The total energy E given by

$$E = \sum_s \rho_s c_{vs} T + \sum_s E_{vs} + \frac{1}{2}\rho u_i u_i + \sum_s \rho_s h_s^\circ \quad (2)$$

the species translational-rotational specific heat at constant volume c_{vs} is given by

$$c_{vs} = c_{vtr\ s} + c_{vrot\ s} \quad (3)$$

the translational and rotational specific heats are given by

$$c_{vtr\ s} = \frac{3}{2}\frac{\hat{R}}{M_s} \qquad c_{vrot\ s} = \frac{\hat{R}}{M_s} \quad (4)$$

where $c_{vrot\ s}$ is zero for monotonic species.

The species vibrational energy is given by

$$E_{vs} = \rho_s \frac{\hat{R}}{M_s}\frac{\theta_{vs}}{\exp(\theta_{vs}/T) - 1} \quad (5)$$

The diffusion models for calculating species diffusion velocity v_s; the calculation of the multicomponent mixture transport coefficients μ, κ, and species diffusivity; and the chemical source terms w_s are described in the following sections.

A. Diffusion Model

Two diffusion models are considered: a Fickian diffusion model, which is used when considering a single binary reaction mechanism, and a more general self-consistent effective binary diffusion model [2] for a mixture of species.

1. Fick's Diffusion Model

In this case, the diffusion of species is given by

$$J_{sj} = \rho_s v_{sj} = -\rho D \frac{\partial c_s}{\partial x_j} \quad (6)$$

where c_s is the mass fraction ρ_s/ρ, and D is the diffusion coefficient, which is equal for all species and given in terms of the Lewis number:

$$D = \frac{\kappa Le}{\rho C_p} \quad (7)$$

2. Multicomponent Diffusion Model

A more accurate representation for a multicomponent mixture is the self-consistent effective binary diffusion (SCEBD) model [2]. This method allows for the variation of species diffusion coefficients.

The effective binary diffusivity for nonelectron pairings is

$$D_s = \left(1 - \frac{\chi_s}{\chi}\right)\left(\sum_{r \neq s}\frac{x_r}{D_{r,s}}\right)^{-1} \quad (8)$$

where x_s is the mole fraction of species s; $D_{r,s}$ is the temperature-dependent binary diffusion transport coefficient, which is described in the following section; and χ_s/χ is the friction coefficient, defined as

$$\frac{\chi_s}{\chi} = \frac{\rho_s/M_s}{\sum_s \rho_s/M_s} \quad (9)$$

To assume nonionization of all species, the mass flux is given by

$$\mathbf{J}_s = \rho_s \mathbf{v}_s = -(cM_sD_s)\nabla(x_s) + \frac{\rho_s}{\rho}\sum(cM_rD_r)\nabla(x_r) \quad (10)$$

where c is the molar density of the gas.

B. Mixture Transport Properties

The transport properties required to solve Eq. (1) are the viscosity, thermal conductivity, and species binary diffusion coefficients. These transport properties depend on the cross sections for collisions between species i and j. The collision integrals provide an accurate representation of the interaction between different particles, molecules, and atoms, as well as ionized species. For a first-order approximation of the Chapman–Enskog theory, we only need to consider the diffusion collision integral $\Omega_{ij}^{1,1}$ and the viscosity collision integral $\Omega_{ij}^{2,2}$.

1. Collision Integrals

Gupta et al. [3] provide curve fits for each collision integral. For collisions not involving charged-particle interaction, the collision integral is given by

$$\pi\Omega_{ij}^{(l,s)}(T) = 10^{-20} D_{ij}^{(l,s)} T^{A_{ij}^{(l,s)}(\ln T)^2 + B_{ij}^{(l,s)}(\ln T)^2 + C_{ij}^{(l,s)}} \quad (11)$$

where $A_{ij}^{(l,s)}$, $B_{ij}^{(l,s)}$, $C_{ij}^{(l,s)}$, and $D_{ij}^{(l,s)}$ are curve-fit coefficients, which can be obtained from Wright et al. [4].

2. Binary Diffusion Coefficients

The binary diffusion transport coefficients appearing in Eq. (8) are defined as

$$D_{r,s} = \frac{3}{16p\pi\Omega_{r,s}^{(1,1)}}\sqrt{\frac{2\pi(k_B T)^3}{\mathcal{M}_{r,s}}} \quad (12)$$

with

$$\mathcal{M}_{i,j} = \frac{M_i M_j}{M_i + M_j} N_A^{-1}$$

3. Multicomponent Mixture Viscosity

The mixture viscosity is given by a second-order multicomponent Gupta et al. [3] method:

$$\mu = \sum_{i=1}^{ns}\left(\frac{x_i M_i/N_A}{\sum_{j=1}^{ns} x_j \Delta_{ij}^{(2)}}\right) \quad (13)$$

where n_s is the number of species and

$$\Delta_{ij}^{(2)} = \frac{16}{5} 1.0 \times 10^{-20}\left(\frac{2M_iM_j}{\pi\hat{R}T(M_i + M_j)}\right)^{1/2}\pi\Omega_{ij}^{(2,2)} \quad (14)$$

4. Multicomponent-Mixture Thermal Conductivity

The mixture's frozen thermal conductivity is calculated from a modified Eucken relation [5]:

$$\kappa = \kappa_{\text{tr}} + \kappa_{\text{int}} \quad (15)$$

where κ_{tr} and κ_{int} are the mixture translational and internal components of the thermal conductivity. These are given by a second-order multicomponent Gupta–Yos method [3,6]:

$$\kappa_{\text{int}} = k_B \sum_{i=1}^{ns}\left[\frac{((c_{pi}/\hat{R}) - \frac{5}{2})x_i}{\sum_{j=1}^{ns} x_j \Delta_{ij}^{(1)}}\right] \quad (16)$$

and $\Delta_{ij}^{(1)}$ is given by

$$\Delta_{ij}^{(1)} = \frac{8}{3} 1.0 \times 10^{-20}\left(\frac{2M_iM_j}{\pi\hat{R}T(M_i + M_j)}\right)^{1/2}\pi\Omega_{ij}^{(1,1)} \quad (17)$$

The translational component of the mixture thermal conductivity is given by

$$\kappa_{\text{tr}} = \frac{15}{4} k_B \sum_{i=1}^{ns}\left(\frac{x_i}{\sum_{j=1}^{ns}\alpha_{ij} x_j \Delta_{ij}^{(2)}}\right) \quad (18)$$

where

$$\alpha_{ij} = 1 + \frac{(1 - (M_i/M_j))(0.45 - 2.54(M_i/M_j))}{(1 + (M_i/M_j))^2} \tag{19}$$

C. Gas-Phase Reactions

We consider two reduced chemical mechanisms with increasing complexity: namely, a simplified two-species mechanism (N_2 and N with Arrhenius parameters [7]) and a five-species mechanism (N_2, O_2, NO, N, and O with Arrhenius parameters [7]). The five-species mechanism represents the realistic reactions of air before ionization happens, which is a good approximation at temperatures less than about 10,000 K. The corresponding equilibrium constants are computed from the Gibbs free energy as functions of temperature and then fitted to Park [7] expressions. For simplicity, ionization and ablation effects are neglected.

1. Two-Species Mechanism

The two-species mechanism includes N_2 and N. Thus, the reaction mechanism is governed by a single dissociation reaction given as

$$\mathrm{N}_2 + \mathrm{M} \rightleftharpoons 2\mathrm{N} + \mathrm{M} \tag{20}$$

where M is a collision partner, either N_2 or N in this case. Let us label this reaction as R_1. The source terms for the species are

$$w_{\mathrm{N}_2} = -w_{\mathrm{N}} = -M_{\mathrm{N}_2} k_f \frac{\rho_{\mathrm{N}_2}}{M_{\mathrm{N}_2}} \left(\frac{\rho_{\mathrm{N}_2}}{M_{\mathrm{N}_2}} + \frac{\rho_{\mathrm{N}}}{M_{\mathrm{N}}} \right) + M_{\mathrm{N}_2} k_b \left(\frac{\rho_{\mathrm{N}}}{M_{\mathrm{N}}} \right)^2 \left(\frac{\rho_{\mathrm{N}_2}}{M_{\mathrm{N}_2}} + \frac{\rho_{\mathrm{N}}}{M_{\mathrm{N}}} \right) \tag{21}$$

The forward and backward Arrhenius reaction rates k_f and k_b are written as

$$k_{fm} = C_{fm} T^{\eta_m} e^{-\theta_{dm}/T} \qquad k_b = k_f / K_{\mathrm{eq}} \tag{22}$$

and the temperature-dependent equilibrium constant K_{eq} is described by Park [7] as

$$K_{\mathrm{eq}} = 10^{-6} \exp(A_1/Z + A_2 + A_3 \ell_n(Z) + A_4 Z + A_5 Z^2) \tag{23}$$

where $Z = 10,000/T$, and A are curve-fit coefficients. The Arrhenius coefficients in Eq. (22) and the curve-fit coefficients in Eq. (23) are given in Tables 1 and 2.

Table 1 Arrhenius parameters for the two-species, one-reaction mechanism [7] and five-species, five-reaction mechanism [7]; corresponding equilibrium constants are computed from the Gibbs free energy as functions of temperature and then fitted to Park [7] expressions

Reaction	C_{fm}, $\mathrm{m}^3/\mathrm{kg\,s}$	η_m	θ_{dm}, K
R_1	1.11d + 16	−1.60d + 00	113,200
R_2	8.25d + 16	−1.00d + 00	59,500
R_3	2.30d + 11	−0.50d + 00	75,500
R_4	3.18d + 07	−0.10d + 00	37,700
R_5	2.16d + 02	1.29d + 00	19,220

2. Five-Species Mechanism

The five-species mechanism includes N_2, O_2, NO, N, and O. Thus, the reaction mechanism is governed by

$$\begin{aligned} &\mathrm{N}_2 + M \rightleftharpoons 2\mathrm{N} + M \qquad \mathrm{O}_2 + M \rightleftharpoons 2\mathrm{O} + M \\ &\mathrm{NO} + M \rightleftharpoons \mathrm{N} + \mathrm{O} + M \qquad \mathrm{N}_2 + \mathrm{O} \rightleftharpoons \mathrm{NO} + \mathrm{N} \\ &\mathrm{NO} + \mathrm{O} \rightleftharpoons \mathrm{O}_2 + \mathrm{N} \end{aligned} \tag{24}$$

Each of these reactions is governed by forward and backward rate coefficients k_{fm} and k_{bm}. Therefore, we write the rate of each reaction as a sum of the forward and backward rates

$$\begin{aligned} \mathcal{R}_1 &= \sum_m \left[k_{b1m} \left(\frac{\rho_{\mathrm{N}}}{M_{\mathrm{N}}} \right)^2 \frac{\rho_m}{M_m} - k_{f1m} \frac{\rho_{\mathrm{N}_2}}{M_{\mathrm{N}_2}} \frac{\rho_m}{M_m} \right] \\ \mathcal{R}_2 &= \sum_m \left[k_{b2m} \left(\frac{\rho_{\mathrm{O}}}{M_{\mathrm{O}}} \right)^2 \frac{\rho_m}{M_m} - k_{f2m} \frac{\rho_{\mathrm{O}_2}}{M_{\mathrm{O}_2}} \frac{\rho_m}{M_m} \right] \\ \mathcal{R}_3 &= \sum_m \left[k_{b3m} \frac{\rho_{\mathrm{N}}}{M_{\mathrm{N}}} \frac{\rho_{\mathrm{O}}}{M_{\mathrm{O}}} \frac{\rho_m}{M_m} - k_{f3m} \frac{\rho_{\mathrm{N}_2}}{M_{\mathrm{N}_2}} \frac{\rho_m}{M_m} \right] \\ \mathcal{R}_4 &= k_{b4} \frac{\rho_{\mathrm{NO}}}{M_{\mathrm{NO}}} \frac{\rho_{\mathrm{N}}}{M_{\mathrm{N}}} - k_{f4} \frac{\rho_{\mathrm{N}_2}}{M_{\mathrm{N}_2}} \frac{\rho_{\mathrm{O}}}{M_{\mathrm{O}}} \\ \mathcal{R}_5 &= k_{b5} \frac{\rho_{\mathrm{O}_2}}{M_{\mathrm{O}_2}} \frac{\rho_{\mathrm{N}}}{M_{\mathrm{N}}} - k_{f5} \frac{\rho_{\mathrm{NO}}}{M_{\mathrm{NO}}} \frac{\rho_{\mathrm{O}}}{M_{\mathrm{O}}} \end{aligned} \tag{25}$$

so that the chemical source terms can be expressed in terms of the individual reaction rates $\mathcal{R}_s$:

$$\begin{aligned} w_{\mathrm{N}2} &= M_{\mathrm{N}2}(\mathcal{R}_2 + \mathcal{R}_4) \qquad w_{\mathrm{O}2} = M_{\mathrm{O}2}(\mathcal{R}_2 - \mathcal{R}_5) \\ w_{\mathrm{NO}} &= M_{\mathrm{NO}}(\mathcal{R}_3 - \mathcal{R}_4 + \mathcal{R}_5) \\ w_{\mathrm{N}} &= M_{\mathrm{N}}(-2\mathcal{R}_1 - \mathcal{R}_3 - \mathcal{R}_4 - \mathcal{R}_5) \\ w_{\mathrm{O}} &= M_{\mathrm{O}}(-2\mathcal{R}_2 - \mathcal{R}_3 + \mathcal{R}_4 + \mathcal{R}_5) \end{aligned} \tag{26}$$

C_{fm}, η_m, and θ_{dm} are given in Table 1.

III. Species Boundary Conditions

The production of species by surface-catalyzed reactions must be balanced by their diffusive flux at the wall:

$$J_{s,w} = w_{s,w} \tag{27}$$

For reactant species, the production rates at the surface can be expressed as recombination coefficient γ_s times the surface impingement fluxes; for O and N, this gives the production rates (negative for loss):

$$w_{\mathrm{O},w} = -\gamma_{\mathrm{O}} \frac{\rho_{\mathrm{O},w} \bar{v}_{\mathrm{O}}}{4} \qquad w_{\mathrm{N},w} = -\gamma_{\mathrm{N}} \frac{\rho_{\mathrm{N},w} \bar{v}_{\mathrm{N}}}{4} \tag{28}$$

where

$$\bar{v}_s = \sqrt{\frac{8\hat{R}T}{\pi M_s}}$$

is the average thermal velocity of species s.

The recombination coefficient is defined as the fraction of impinging reactant flux removed permanently from the gas phase. It is not a fundamental chemical quantity; rather, it reflects the total

Table 2 Equilibrium constants computed from the Gibbs free energy as functions of temperature and then fitted to Park [7] expressions

Case	A_1	A_2	A_3	A_4	A_5
R1	1.60600d + 00	−1.57320d + 00	1.39230d + 00	−1.15530d + 01	−4.54300d − 3
R2	6.41830d − 01	2.42530d + 00	1.90260d + 00	−6.6277d + 00	3.51510d − 02
R3	6.38170d − 01	6.81890d − 01	6.63360d − 01	−7.57730d + 00	−1.10250d − 02
R4	9.67940d − 01	8.91310d − 01	7.29100d − 01	−3.95550d + 00	6.48800d − 03
R5	−3.73200d − 03	−1.74340d + 00	−1.23940d + 00	−9.49520d − 01	−1.46341d − 01

efficiency of all operating surface reaction pathways that remove species s on a particular combination of temperature, pressure, and gas composition. If the reactant species is consumed to produce more than one product species, branching fractions $f_{s,r}$ can be defined as the fraction of impinging reactant removed permanently from the gas phase that participates in forming product species r.

The absolute lower and upper bounds on both γ_s and $f_{s,r}$ are 0 and 1, but this range may be reduced by other factors such as the availability of partner reactants. For a partially dissociated gas mixture of oxygen and nitrogen interacting with a catalytic surface via three net steady-state heterogeneous reaction pathways ($O + O \rightarrow O_2$, $N + N \rightarrow N_2$, and $O + N \rightarrow NO$), element conservation dictates the constraint:

$$(1 - f_{O,O_2}) \frac{\gamma_O \rho_{O,w} \bar{v}_O}{M_O} = (1 - f_{N,N_2}) \frac{\gamma_N \rho_{N,w} \bar{v}_N}{M_N} \tag{29}$$

The individual production rates of the surface reaction products are

$$\begin{aligned} w_{O_2,w} &= -f_{O,O_2} \frac{M_{O_2}}{2M_O} w_{O,w} \qquad w_{N_2,w} = -f_{N,N_2} \frac{M_{N_2}}{2M_N} w_{N,w} \\ w_{NO,w} &= (f_{N,N_2} - 1) \frac{M_{NO}}{2M_N} w_{N,w} = (f_{O,O_2} - 1) \frac{M_{NO}}{2M_O} w_{O,w} \end{aligned} \tag{30}$$

where the recombination coefficient and branching factor of species are obtained from experiments.

IV. Numerical Method

We solve the equations governing unsteady fluid motion in conservative form: namely, the conservative form of the chemical species mass, momentum, and energy equations. In DNS, the equations are solved with no modeling assumption. Thus, DNS allows for the accurate and detailed simulation of fluid flows in the laminar-to-turbulent regimes. Turbulent flow calculations are significantly more challenging than their laminar counterparts, as all turbulent length and time scales must be resolved.

The spatial convective derivatives are computed using a fourth-order-accurate, bandwidth-optimized, weighted essentially non-oscillatory (WENO) scheme [8–10], which is a high-order shock-capturing scheme. To perform the numerical integration, we use a third-order-accurate low-storage Runge–Kutta method by Williamson [11]. The viscous terms are computed using a fourth-order-accurate central scheme. A Newton–Raphson method is used to obtain the temperature from Eq. (2).

V. Code Validation

A. Similarity Solution for Compressible Laminar Flow

A similarity solution can be obtained by performing a similarity transformation of the partial differential boundary-layer equations to transform them to ordinary differential equations (ODEs) [12].

The governing equations for a zero-pressure-gradient laminar compressible boundary layer are

$$\begin{aligned} &\frac{\partial \rho^* u^*}{\partial x^*} + \frac{\partial \rho^* v^*}{\partial y^*} = 0 \\ &\rho^* u^* \frac{\partial u^*}{\partial x^*} + \rho^* v^* \frac{\partial u^*}{\partial y^*} = \frac{\partial}{\partial y^*} \left(\mu^* \frac{\partial u^*}{\partial y^*} \right) \\ &\rho^* u^* \frac{\partial h^*}{\partial x^*} + \rho^* v^* \frac{\partial h^*}{\partial y^*} = \frac{\partial}{\partial y^*} \left(\kappa^* \frac{\partial T^*}{\partial y^*} \right) + \mu^* \left(\frac{\partial u^*}{\partial y^*} \right)^2 \end{aligned}$$

In this section only, the superscript $*$ means dimensional quantities and v is the velocity in the wall-normal direction. Nondimensionalize this set of equations using the following scales:

$$u = \frac{u^*}{U_\infty} \qquad \rho = \frac{\rho^*}{\rho_\infty} \qquad T = \frac{T^*}{T_\infty} \qquad h = \frac{h^* - h^*_\infty}{\frac{1}{2} U^2_\infty} \qquad \mu = \frac{\mu^*}{\mu_\infty}$$

where $h^*_\infty = C_p T_\infty$. Also introduce the transformation used in the incompressible boundary layer:

$$\eta = \frac{y}{x} \sqrt{Re_x}$$

where

$$Re_x = \frac{\rho_\infty U_\infty x}{\mu_\infty}$$

Assume

$$\rho u = \frac{u}{T} = f(\eta)$$

From the continuity equation, we can get

$$\rho v = \frac{1}{2\sqrt{Re_x}} [\eta f - g(\eta)]$$

where

$$g(\eta) = \int_0^\eta f(\eta) \mathrm{d}\eta$$

From momentum and energy equations, we can get

$$\frac{\partial}{\partial \eta} \left(\mu \frac{\partial u}{\partial \eta} \right) + \frac{1}{2} g(\eta) \frac{\partial u}{\partial \eta} = 0 \tag{31}$$

$$\frac{1}{2} g(\eta) \frac{\partial h}{\partial \eta} = -\frac{1}{Pr} \frac{\partial}{\partial \eta} \left(\mu \frac{\partial h}{\partial \eta} \right) - 2\mu \left(\frac{\partial u}{\partial \eta} \right)^2 \tag{32}$$

where $Pr = \mu C_p / \kappa$.

The preceding set of ODEs can be cast into a first-order system of ODEs:

$$\begin{aligned} &\frac{du}{d\eta} = \frac{F}{\mu} \qquad \frac{dF}{d\eta} = \frac{1}{2} \frac{g(\eta)}{\mu} F \qquad \frac{dh}{d\eta} = \frac{Pr}{\mu} G \\ &\frac{dG}{d\eta} = -\frac{1}{2} \frac{Pr}{\mu} G g - 2 \frac{F^2}{\mu} \qquad \frac{dg}{d\eta} = \frac{u}{T} \end{aligned}$$

This first-order system can be solved by generic ODE solvers with one of the following boundary conditions:

1) In the adiabatic boundary condition, if $\eta = 0$, then $u = 0$, $G = 0$, and $g = 0$, and if $\eta = \infty$, then $u = 1$ and $h = 1$.

2) In the isothermal boundary condition, if $\eta = 0$, then $u = 0$,

$$h = \frac{2(T_w / T_\infty - 1)}{(\gamma - 1) Ma^2_\infty}$$

and $g = 0$, and if $\eta = \infty$, then $u = 1$ and $h = 1$.

The results of the DNS code can be compared with this similarity solution by turning off the gas-phase reactions and specifying heat capacity ratio $\gamma = \text{const}$ and $Pr = \text{const}$ and letting $\mu \propto T^\omega$.

Figure 1 plots nondimensional velocity across the boundary layer with $T_\infty / T_w = 1.0$, $\mu / \mu_\infty = (T / T_\infty)^{0.666}$, $Pr = 0.71$, and $\gamma = 1.4$ for freestream Mach numbers 2, 3, 4, and 5. The number of grid points for numerical results is 100×100 in the streamwise and wall-normal directions, respectively. There is good agreement between the numerical results and the similarity solution. The minor discrepancy is due to the leading-edge shock that is present in the numerical solution and not in the similarity solution.

B. Reacting Laminar Boundary Layer

The constitutive relations and finite-rate gas-phase reaction in the DNS code are validated against DPLR [1] solutions. For flow over a flat plate with a freestream Mach number of 4, $Le = 1.0$, a noncatalytic isothermal wall with $T_\infty / T_w = 1.0$, and a gas-phase reaction with $N_2 + M \rightleftharpoons 2N + M$, Fig. 2 plots the nondimensional velocity and temperature profiles. The Gupta–Yos mixing rule [3,6] is used for mixture transport properties. Grid convergence studies are performed and the number of grid points for both DNS and DPLR results is 100×100 in the streamwise and wall-normal directions, respectively. Good agreement is found between the DPLR and DNS code solutions.

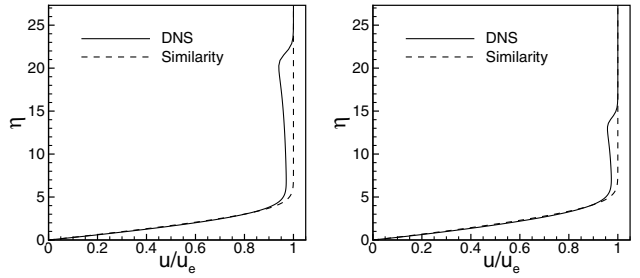

a) $Ma_\infty = 2.0$ b) $Ma_\infty = 3.0$

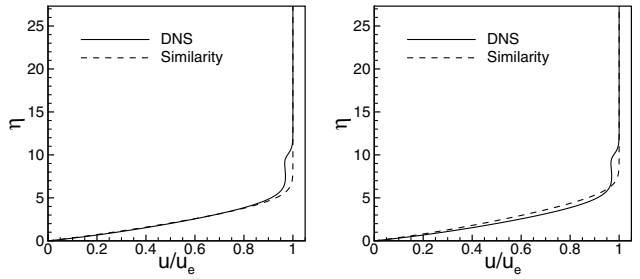

c) $Ma_\infty = 4.0$ d) $Ma_\infty = 5.0$

Fig. 1 Comparison of the numerical and similarity solutions with $Pr = 0.71$ and the isothermal wall with $T_\infty/T_w = 1$ and $\mu \propto T^{0.666}$ for different freestream Mach numbers.

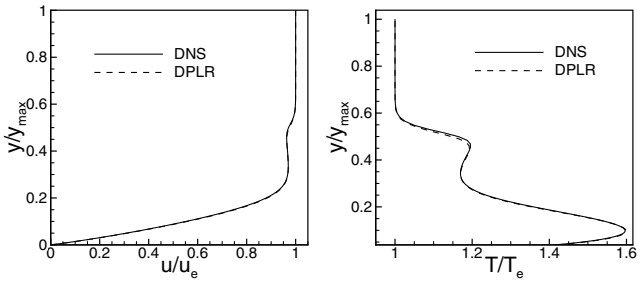

a) Velocity profile b) Temperature profile

Fig. 2 Comparison of the numerical and similarity solutions with $Ma_\infty = 4$ and $Le = 1$ and the noncatalytic isothermal wall with $T_\infty/T_w = 1$ and $Re_\infty = 1000$.

C. Surface Reaction Validation

1. Diffusion-Tube Sidearm Reactor

The diffusion-tube sidearm reactor [13] in conjunction with laser-induced fluorescence for species diagnostics has served as the main method to measure O and N atom recombination coefficients in the range of 300 to 1000 K. The diffusion tube consists of a dead-end sidearm tube connected at right angles to a main flow tube (see Fig. 3). Free-radical species are produced in the main flow tube upstream of the tube intersection, typically by dissociating molecular gases using some type of low-pressure electrical discharge. The dissociated species flow past the opening of the sidearm tube. As the reactants

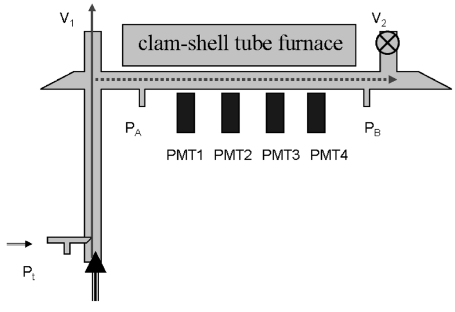

Fig. 3 Schematic diagram of a diffuse-tube sidearm reactor.

diffuse into the sidearm tube, they are progressively removed from the gas phase by surface reactions on the wall, establishing a unique steady-state species-concentration profile down the length of the tube. This reactor design simplifies subsequent data analysis because gas transport in the sidearm is restricted to species diffusion.

A surface chemistry model is needed to fit experimental data by adjusting the model parameters to reproduce experimental results. In the case of binary atom-molecule system, assuming a purely catalytic wall and a single heterogeneous loss pathway leading to atom recombination, one simple reaction-diffusion model that can be applied to evaluate surface recombination is obtained by solving the linear one-dimensional diffusion equation with surface loss included as a first-order sink term:

$$D\frac{\partial^2 n}{\partial x^2} - \dot{R}_{\text{sink}} = 0 \tag{33}$$

where $\dot{R}_{\text{sin}\,k} \equiv$ the recombination coefficient times the atom surface impingement rate times the surface area per volume, or

$$\dot{R}_{\text{sink}} = \gamma\left(\frac{\bar{v}n}{4}\right)\left(\frac{2\pi R dx}{\pi R^2 dx}\right) = \left(\frac{\gamma\bar{v}}{2R}\right)n \tag{34}$$

with boundary conditions at the tube entrance and tube end:

$$n(0) = n_0 \qquad D\frac{dn}{dx}(L) = -\gamma\frac{\bar{v}n(L)}{4} \tag{35}$$

where n is the atom number density, x is the axial tube coordinate, R is the tube radius, and L is the length of the tube. A simple analytic solution can be obtained from Eqs. (34) and (35):

$$\frac{n(x)}{n(0)} = \cosh(\alpha x) - \frac{\alpha\sinh(\alpha L) + \beta\cosh(\alpha L)}{\alpha\cosh(\alpha L) + \beta\sinh(\alpha L)}\sinh(\alpha x) \tag{36}$$

where

$$\alpha = \sqrt{\frac{\gamma\bar{v}}{2RD}} \qquad \beta = \frac{\gamma\bar{v}}{4D}$$

2. Numerical Results

The numerical solution can be obtained from the DNS code by neglecting the momentum and energy equations and solving continuity equations in cylindrical form with zero convective velocity and chemical source terms, which are reduced to

$$\frac{1}{r}\frac{\partial}{\partial r}(rj_{sr}) + \frac{\partial}{\partial x}(j_{sx}) = 0 \tag{37}$$

where j_{sr} and j_{sx} are the diffusive mass fluxes in the radial and axial directions, which are computed by SCEBD, described in Sec. II, and the surface boundary conditions are described in Sec. III.

Figure 4 gives the comparison of the numerical results with analytic results described in [1] at $T = 298$ K and $P = 0.45$ torr for $\gamma = 10^{-6}, 5\times10^{-6}, 10^{-5}$, and 5×10^{-5}. These values are typical of diffusion-tube sidearm-reactor experiments in Stanford Research Institute (SRI). The computation domain is also chosen to be the same as the sidearm-reactor geometry in SRI, with tube length $L = 146.7$ cm and uniform radius $R = 1.1$ cm, closed at one end by a disk normal to the tube axis. The number of grid points is 120×20 in the axial and radius directions, respectively.

D. Turbulence Validation

1. Empirical Predictions and Experimental Data

Turbulence can be validated against empirical predictions and detailed experimental data. Figure 5 plots the van Driest transformed velocity profiles in turbulent boundary layers for DNS, varying the freestream Mach number and wall-temperature condition [14,15]. The symbols show the theoretical values, illustrating the good accuracy of the simulations. An index of the flow accuracy at the wall is given by the skin-friction coefficient C_f. Figure 6 plots C_f for the same simulations relative to the empirical predictions [16]. The error bars show a 7% error, for which the error in the empirical prediction

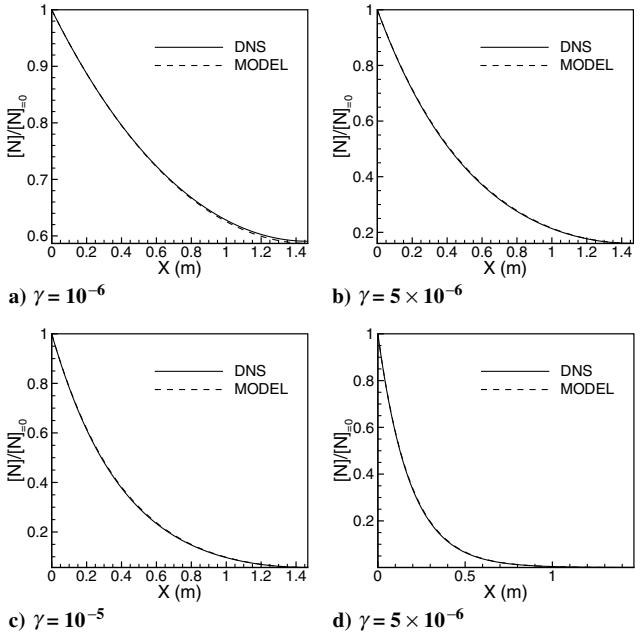

Fig. 4 Scaled nitrogen atom concentration along the diffusion tube at temperature $T = 298$ K, pressure $P = 0.45$ torr with different recombination coefficients.

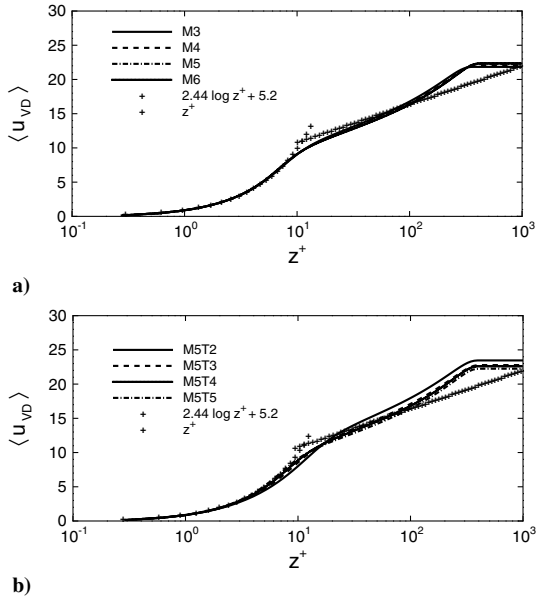

Fig. 5 Van Driest transformed velocity in turbulent boundary layers varying a) freestream Mach number from [14,15] and b) wall temperature for DNS from [15].

is 10%. Figure 6 further illustrates the accuracy of the simulations (specifically, at the wall). This degree of accuracy is necessary to study the interaction between the boundary-layer flow and gas phase and the surface chemistry. Figure 7 illustrates good agreement between DNS results and experimental data [17,18] for a turbulent boundary layer with Mach 2 and $Re_\theta = 4492$. The number of grid points used to achieve the preceding results is $384 \times 256 \times 107$ in the streamwise, spanwise, and wall-normal directions, respectively. The flow initialization, the choice of domain size, and grid resolution for DNS are discussed by Martin [14].

2. *Linear Stability Comparison*

To assess how well fluctuations about a mean flow are represented, an additional test is to simulate spatially growing instabilities using

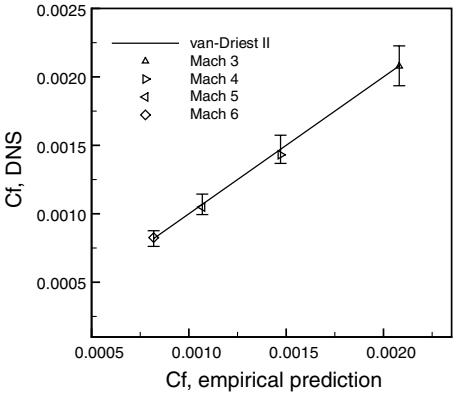

Fig. 6 Skin-friction coefficient for hypersonic turbulent boundary layer from DNS (flow conditions are as in Fig. 5a).

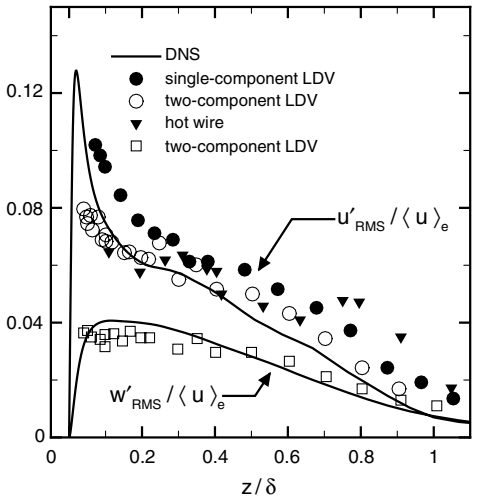

Fig. 7 Velocity fluctuations in turbulent boundary layers at Mach 2 and Re_θ 4492: DNS data (lines) and experimental data [17,18] (symbols); LDV denotes laser Doppler velocimetry and RMS denotes root mean square.

DNS and compare the results with those given by linear stability theory, as described in the Appendix. The laminar mean flow is superimposed with an eigenfunction of the linearized Navier–Stokes equations, which is a spatially evolving instability wave. For low amplitudes, the instability should evolve in accordance with linear theory. The growth rate that is observed in the DNS is required to match linear theory [12].

The parameters of the base flow and the eigenmode used in Fig. 8 are listed in Table 3. The size of the computational domain of DNS is 14δ in the streamwise direction and 7δ in the wall-normal direction. The number of grid points is 384×140 in the streamwise and wall-normal directions, respectively. At the inlet, the laminar mean profile obtained from the two-dimensional boundary-layer equations is prescribed, and disturbances obtained from solving the linear stability equations are added at the inlet. At the outlet, a supersonic

Table 3 Parameters of the base flow and the eigenmode used for simulation in Fig. 8

Parameters	Values
M	4.5
Re_x	10^6
ω	0.225
α_r	0.246
α_i	−0.00273
A[a]	10^{-4}

[a]The amplitude of the fluctuations.

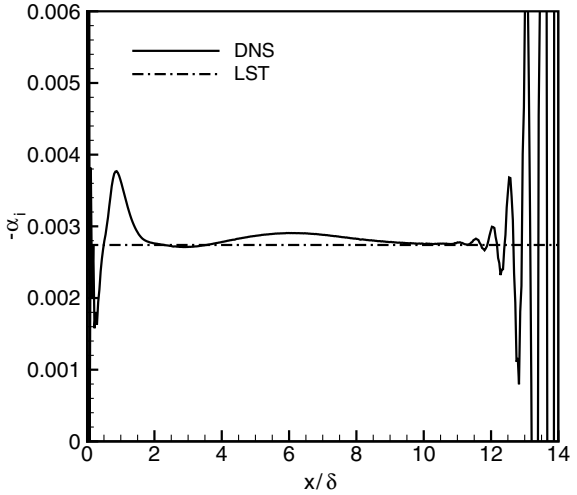

Fig. 8 Local growth rate given by the DNS code and linear stability theory (LST).

exit condition is used. The simulation is continued for about 20 flow-through times to let the disturbance evolve spatially.

Figure 8 plots the local growth rate computed from the streamwise velocity disturbance at $z = 0.2\delta$ given by the DNS and the linear stability theory. The error is very large within a 2δ region near the inlet and the outlet, in which we are not assessing the accuracy of the growth ratio, due to interference with the specified boundary condition. For the region of interest in the middle of the domain, the maximal relative error is 5.8%.

To give a more quantitative measurement of the agreement between the DNS and linear stability results, we define the correlation r between the computed perturbation field q'_{DNS} and the corresponding field from the linear stability analysis, q'_{LSA}, by [19]

$$r = \frac{\langle q'_{\mathrm{DNS}} q'_{\mathrm{LSA}} \rangle}{\langle q'^2_{\mathrm{DNS}} \rangle^{1/2} \langle q'^2_{\mathrm{LSA}} \rangle^{1/2}}$$

where q a flowfield quantity and

$$\langle \cdot \rangle = \int_V \cdot d\mathbf{x}$$

is the integral over the whole computational domain. By letting q' be the streamwise velocity perturbation, we get $r = 0.9571$.

The error may seem large. However, this is a rather stringent test because the disturbance level is of the order of 10^{-4}. This test is usually done with high-order central differencing schemes, and errors of 1–2% can be achieved. In our case, a shock-capturing scheme is needed in the DNS, and the results given by WENO in Fig. 8 are considered to be satisfactory.

VI. Conclusions

This paper describes a systematic validation procedure for testing DNS codes for wall-bounded turbulence, including finite-rate gas-phase and surface reactions. Mean flowfield, surface boundary conditions, and turbulence are tested separately. The validation of our DNS code using this procedure shows the effectiveness of this procedure and it may serve as a guideline for testing DNS codes of such a category.

Appendix: Linear Stability Equations for Compressible Flows

With the assumption that the base flow is parallel and that the disturbance is of the following form,

$$q'(x, y, z, t) = \hat{q}(y) e^{i(\alpha x + \beta z - \omega t)} \tag{A1}$$

the linear stability equations for compressible flows can be written as

$$\frac{df_i}{dy} = \sum_{j=1}^{8} a_{ij} f_j \qquad j = 1 - 8 \tag{A2}$$

Details about the derivation can be found in [12]. Here, x, y, and z are the streamwise, wall-normal, and spanwise directions, respectively. Equation (A2) is the set of linear stability equations with

$$f_1 = \alpha\hat{u} + \beta\hat{w} \qquad f_2 = \alpha\frac{d\hat{u}}{dy} + \beta\frac{d\hat{w}}{dy} \qquad f_3 = \hat{v} \qquad f_4 = \frac{\hat{p}}{\gamma M^2}$$

$$f_5 = \hat{T} \qquad f_6 = \frac{d\hat{T}}{dy} \qquad f_7 = \alpha\hat{u} - \beta\hat{w} \qquad f_8 = \alpha\frac{d\hat{u}}{dy} - \beta\frac{d\hat{w}}{dy}$$

The nonzero coefficients of Eq. (A2) are

$$a_{12} = 1$$

$$a_{21} = \frac{iRe}{\mu T} b_1 + b_2 \qquad a_{22} = -\frac{1}{\mu}\frac{d\mu}{dT}\frac{dT}{dy}$$

$$a_{23} = \frac{Reb_3}{\mu T} - b_2\frac{dT}{dy}\left(\frac{i}{\mu}\frac{d\mu}{dT} + \frac{1+2d}{3}\frac{i}{T}\right)$$

$$a_{24} = \frac{iReb_2}{\mu T} - \frac{1+2d}{3}\gamma M^2 b_1 b_2$$

$$a_{25} = \frac{1+2d}{3T} b_1 b_2 - \frac{1}{\mu}\frac{d\mu}{dT}\left(\alpha\frac{d^2U}{dy^2} + \beta\frac{d^2W}{dy^2}\right) - \frac{1}{\mu}\frac{d^2\mu}{dy^2}\frac{dT}{dy} b_3$$

$$a_{26} = -\frac{1}{\mu}\frac{d\mu}{dT} b_3 \qquad a_{31} = -i \qquad a_{33} = \frac{1}{T}\frac{dT}{dy}$$

$$a_{34} = -i\gamma M^2 b_1 \qquad a_{35} = \frac{ib_1}{T}$$

$$a_{41} = -\frac{i}{E}\left[-2a_{22} + \frac{2}{3}(2+d)a_{33}\right] \qquad a_{42} = -\frac{i}{E}$$

$$a_{43} = \frac{1}{E}\left[-b_2 + \frac{2(2+d)}{3\mu T}\frac{d\mu}{dT}\left(\frac{dT}{dy}\right)^2 + \frac{2(2+d)}{3T}\frac{d^2T}{dy^2} - \frac{iReb_1}{\mu T}\right]$$

$$a_{44} = -\frac{2i}{3E}(2+d)\left(-b_1 a_{22} + b_3 + \frac{1}{T}\frac{dT}{dy} b_1\right)\gamma M^2$$

$$a_{45} = \frac{i}{E}\left[\frac{1}{\mu}\frac{d\mu}{dT} b_3 + \frac{2(2+d)}{3T}(-a_{22} b_1 + b_3)\right]$$

$$a_{46} = \frac{2i}{3ET}(2+d)b_1, \qquad a_{56} = 1$$

$$a_{62} = -2(\gamma-1)PrM^2\left(\frac{b_3}{b_2}\right)$$

$$a_{63} = \frac{PrRe}{\mu} a_{33} - 2i(\gamma-1)PrM^2 b_3$$

$$a_{64} = -\frac{i}{\mu}(\gamma-1)PrReM^2 b_1$$

$$a_{65} = i\frac{PrRe}{\mu T} b_1 + b_2 - \frac{1}{\kappa}\frac{d\kappa}{dT}\frac{d^2T}{dy^2} - \frac{1}{\kappa}\frac{d^2\kappa}{dT^2}\left(\frac{dT}{dy}\right)^2 - (\gamma-1)PrM^2\frac{1}{\mu}\frac{d\mu}{dT}\left[\left(\frac{dU}{dy}\right)^2 + \left(\frac{dW}{dy}\right)^2\right]$$

$$a_{66} = -\frac{2}{\kappa}\frac{d\kappa}{dT}\frac{dT}{dy} \qquad a_{68} = -\frac{2(\gamma-1)}{b_2} PrM^2 b_4 \qquad a_{78} = 1$$

$$a_{83} = \frac{Reb_4}{\mu T} \qquad a_{85} = -\frac{1}{\mu}\frac{d\mu}{dT}\left(\alpha\frac{d^2W}{dy^2} - \beta\frac{d^2U}{dy^2}\right) - \frac{1}{\mu}\frac{d^2\mu}{dT^2}\frac{dT}{dy} b_4$$

$$a_{86} = -\frac{1}{\mu}\frac{d\mu}{dT} b_4 \qquad a_{87} = \frac{iReb_1}{\mu T} + b_2 \qquad a_{88} = a_{22} \tag{A3}$$

where

$$b_1 = \alpha U + \beta W - \omega \qquad b_2 = \alpha^2 + \beta^2 \qquad b_3 = \alpha\frac{dU}{dy} + \beta\frac{dW}{dy}$$

$$b_4 = \alpha\frac{dW}{dy} - \beta\frac{dU}{dy} \qquad d = \frac{\lambda}{\mu}$$

and

$$E = \frac{Re}{\mu} + \frac{2}{3} i(2+d)\gamma M^2 b_1$$

where $i = \sqrt{-1}$, and λ is the bulk viscosity, which is set to zero. All of the preceding equations are nondimensionalized. The boundary conditions for Eq. (A2) are

$$\begin{cases} f_1 = f_3 = f_5 = f_7 = 0, & y = 0 \\ f_1 = f_3 = f_5 = f_7 = 0, & y \to \infty \end{cases} \tag{A4}$$

The linear stability equations can be solved by boundary-value problem solvers such as bvp4c provided by MATLAB.

Acknowledgments

This work is sponsored in part by the U.S. Air Force Office of Scientific Research under grant FA9550-05-1-0490 and NASA cooperative agreements NNX08AD04A and NCC3-989. Computational resources are provided by the Cluster for Research on Complex Computation (CRoCCo) Laboratory at Princeton University.

References

[1] Wright, M. J., Candler, G. V., and Bose, D., "Data-Parallel Line Relaxation Method for the Navier-Stokes Equations," *AIAA Journal*, Vol. 36, No. 9, 1998, pp. 1603–1609. doi:10.2514/2.586

[2] Ramshaw, J. D., "Self-Consistent Effective Binary Diffusion in Multicomponent Gas Mixtures," *Journal of Non-Equilibrium Thermodynamics*, Vol. 15, No. 3, 1990, pp. 295–300.

[3] Gupta, R. N., Yos, J. M., Thompson, R. A., and Lee, K.-P., "A Review of Reaction Rates and Thermodynamic Transport Properties for an 11-Species Air Model for Chemical and Thermal Nonequilibrium Calculations to 30,000 K," NASA RP-1232, 1990.

[4] Wright, M. J., Levin, E., and Bose, D., "Recommended Collision Integrals for Transport Property Computations 1: Air Species," *AIAA Journal*, Vol. 43, No. 12, 2005, pp. 2558–2563. doi:10.2514/1.16713

[5] Hirschfelder, J. O., "Heat Conductivity in Polyatomic or Electronically Excited Gases 2," *Journal of Chemical Physics*, Vol. 26, No. 2, 1957, pp. 282–285. doi:10.1063/1.1743285

[6] Yos, J. M., "Transport Properties of Nitrogen, Hydrogen, Oxygen, and Air to 30,000 K," Avco Corp., TR AD-TM-63-7, Wilmington, MA, 1963.

[7] Park, C., *Nonequilibrium Hypersonic Aerodynamics*, Wiley, New York, 1990.

[8] Weirs, V. G., and Candler, G. V., "Optimization of Weighted ENO Schemes for DNS of Compressible Turbulence," AIAA Paper 1997-1940, 1997.

[9] Taylor, E. M., Wu, M., and Martin, M. P., "Optimization of Nonlinear Error Sources for Weighted Nonoscillatory Methods in Direct Numerical Simulations of Compressible Turbulence," *Journal of Computational Physics*, Vol. 223, No. 1, 2007, pp. 384–397. doi:10.1016/j.jcp.2006.09.010

[10] Martin, M. P., Taylor, E. M., Wu, M., and Weirs, V. G., "A Bandwidth-Optimized WENO Scheme for the Effective Direct Numerical Simulation of Compressible Turbulence," *Journal of Computational Physics*, Vol. 220, No. 1, 2006, pp. 270–289. doi:10.1016/j.jcp.2006.05.009

[11] Williamson, J. H., "Low-Storage Runge-Kutta Schemes," *Journal of Computational Physics*, Vol. 35, No. 1, 1980, pp. 48–56. doi:10.1016/0021-9991(80)90033-9

[12] Mack, L. M., "Boundary-Layer Linear Stability Theory, Special Course on Stability and Transition of Laminar Flow," AGARD, TR R709, Neuilly-sur-Seine, France, 1984.

[13] Smith, W. V., "The Surface Recombination of H Atoms and OH Radicals," *Journal of Chemical Physics*, Vol. 11, Mar. 1943, pp. 110–125. doi:10.1063/1.1723811

[14] Martin, M. P., "DNS of Hypersonic Turbulent Boundary Layers Part 1: Initialization and Comparison with Experiments," *Journal of Fluid Mechanics*, Vol. 570, Jan. 2007, pp. 347–364. doi:10.1017/S0022112006003107

[15] Martin, M. P., "DNS of Hypersonic Turbulent Boundary Layers," 34th AIAA Fluid Dynamics Conference, AIAA Paper 2004-2337, 2004.

[16] Van-Driest, E., "Problem of Aerodynamic Heating," *Aeronautical Engineering Review*, Vol. 15, No. 10, Oct. 1956, pp. 26–41.

[17] Debiève, J. F., Gouin, H., and Gaviglio, J., "Momentum And Temperature Fluxes in a Shock Wave-Turbulence Interaction," *Structure of Turbulence in Heat and Mass Transfer*, Hemisphere, Washington, D.C., 1982, pp. 277–296.

[18] Eléna, M., and Lacharme, J. P., "Experimental Study of a Supersonic Turbulent Boundary Layer Using a Laser Doppler Anemometer," *Journal de Mécanique Théorique et Appliquée*, Vol. 7, No. 2, 1988, p. 175.

[19] Matheou, G., Pantano, C., and Dimotakis, P. E., "Verification of a Fluid-Dynamics Solver Using Correlations with Linear Stability Results," *Journal of Computational Physics*, Vol. 227, No. 11, 2008, pp. 5385–5396. doi:10.1016/j.jcp.2008.01.055

T. Jackson
Associate Editor